

# Separation of manganese isotopes by resonance ionization mass spectrometry for $^{53}\text{Mn}$ half-life determination

Nina Kneip<sup>1,\*</sup>, Dominik Studer<sup>1</sup>, Tom Kieck<sup>2,3</sup>, Jiri Ulrich<sup>4</sup>, Rugard Dressler<sup>4</sup>, Dorothea Schumann<sup>4</sup> and Klaus Wendt<sup>1</sup>

<sup>1</sup> Institut für Physik, Johannes Gutenberg-Universität Mainz, 55099 Mainz, Germany

<sup>2</sup> GSI Helmholtzzentrum für Schwerionenforschung GmbH, 64291 Darmstadt, Germany

<sup>3</sup> Helmholtz Institut Mainz, Staudingerweg 7, 55128 Mainz, Germany

<sup>4</sup> Paul Scherrer Institut, Forschungsstrasse 111, 5232 Villigen PSI, Switzerland

Received: 29 November 2021 / Received in final form: 14 January 2022 / Accepted: 17 January 2022

**Abstract.** We report on the production of ultra-pure samples of the long-lived radioisotope  $^{53}\text{Mn}$  for precision measurements of its half-life. Activated samples from a copper beam dump from PSI, which was irradiated with 590 MeV protons, were used for extraction of the manganese fraction. Following initial radiochemical purification, efficient three-photon laser resonance ionization of manganese inside a hot-cavity laser ion source was applied for subsequent isotope selection in a 30 keV high transmission magnetic mass separator. A new ionization scheme was developed and characterized for  $^{53}\text{Mn}$  implantation. In this way the isobar  $^{53}\text{Cr}$  and the Mn isotopes  $^{54,55}\text{Mn}$  are quantitatively removed, with a special focus on the radioactive  $^{54}\text{Mn}$  isotope. Microgram quantities of  $^{53}\text{Mn}$  were implanted into Al targets with an isotopic and isobaric purity of well above  $10^3$ . An overall efficiency of the enrichment process of about 15% was demonstrated.

## 1 Introduction

The genesis of the elements started within the first 3 min after the big bang, when H up to Be was formed. All elements heavier than Be were and still are produced by the various processes of stellar nucleosynthesis. Up to Fe they are synthesized by hydrostatic nuclear fusion in star cores [1]. Elements beyond iron and nickel are formed in various astrophysical scenarios that are not yet fully understood. The occurrence of nuclides with half-lives of the order of 100 ka to 10 Ma in astronomical objects and in some particular locations on the Earth allows to study the origin of matter in the Solar system.  $^{53}\text{Mn}$  is one of the proton-rich isotopes in the iron peak region which is supposed to be produced during supernovae explosions. Because of its long half-life in the order of 3.8(4) Ma [2,3],  $^{53}\text{Mn}$  is of particular interest of stellar evolution studies. It belongs to a group of about 10 so-called short lived cosmogenic radionuclides with half-lives in the range of 100 ka to 100 Ma, which also include  $^{10}\text{Be}$ ,  $^{26}\text{Al}$ ,  $^{41}\text{Ca}$ ,  $^{60}\text{Fe}$ ,  $^{129}\text{I}$ ,  $^{107}\text{Pd}$ ,  $^{146}\text{Sm}$ ,  $^{182}\text{Hf}$  and  $^{244}\text{Pu}$ . All these isotopes were present during the formation of our Solar system. By studying extraterrestrial material or terrestrial archives, highly relevant information can be obtained about the processes within and the composition of the early Solar system [4]. Additionally, small amounts of these isotopes reach the earth in form of the high-energy nuclei component of galactic cosmic rays (HZE ions), as interstellar dust particles from extrasolar sources or are continuously produced by spallation reactions on

the Earth surface [5]. Sensitive isotope ratio measurements on primarily the heavier ones of these isotopes, as well as  $^{53}\text{Mn}$ , are carried out at specific large scale accelerator mass spectrometry (AMS) facilities. High acceleration energy of 10 MeV and beyond is required in order to minimize background and achieve sufficient isotopic and isobaric selectivity [6,7]. A broad collection of AMS based measurements on  $^{53}\text{Mn}$  abundances are reported. These concern both, extra-terrestrial materials [8] as well as various terrestrial sources, including exposure age dating in surface rocks of Australia or Antarctica [9,10] or deep-sea crusts [11]. Within the latter, the detected  $^{53}\text{Mn}$  is clearly identified as supernova remnants on Earth [12]. Alternatively, the occurrence of  $^{53}\text{Mn}$  in the early Solar system is verified via quantification of the excess of its decay product  $^{53}\text{Cr}$  in  $^{53}\text{Mn}/^{53}\text{Cr}$  dating [13]. As pointed out in [14], this  $^{53}\text{Mn}/^{53}\text{Cr}$  chronometer can well be utilized to accurately date events in the early Solar system. However, such studies require precise data on the  $^{53}\text{Mn}$  half-life as well as on its neutron capture cross sections in order to obtain conclusive information on pathways regarding its formation in stellar events and its deposition on Earth. Similar as for few others of the short-lived cosmogenic isotopes, these data are not known with acceptable uncertainty and more precise measurements are needed. In the case of  $^{53}\text{Mn}$ , the uncertainty of the half-life is 10%. This uncertainty should be reduced to values well below 3% in order to utilize  $^{53}\text{Mn}$  for precise dating both of terrestrial and extraterrestrial samples. Due to its extremely low abundance together with its long half-life in the order of Ma and its low energy electron capture decay, no simple decay measurements can be used for the determination of

\* e-mail: [nina.kneip@uni-mainz.de](mailto:nina.kneip@uni-mainz.de)

the half-life of  $^{53}\text{Mn}$  for obvious reasons. Instead, the half-life can be determined only with, reasonably strong and well quantified  $^{53}\text{Mn}$  samples of highest purity, using the fundamental relation:

$$T_{\frac{1}{2}} = \ln(2) \frac{N}{A} \quad (1)$$

where  $T_{\frac{1}{2}}$  denotes the half-life, and  $N$  and  $A$  the number of atoms and the activity of the radioactive isotope in the given sample, respectively.

In the scope of the foreseen half-life measurements, multi-collector inductively coupled plasma mass spectrometry (MC-ICP-MS) will be used for the accurate determination of the number of atoms of  $^{53}\text{Mn}$ . A precision of better than 0.5% has been demonstrated [15]. As  $^{53}\text{Mn}$  is a pure electron capture (EC) radionuclide, its decay is accompanied only by emission of low-energy secondary Auger electrons and X-rays in the energy range of few keV. This restricts the number of suitable activity measurement techniques considerably; liquid scintillation counting (LSC) is commonly used for the activity quantification of this class of radionuclides and will be utilized during this project as well [16]. Both MC-ICP-MS and LSC have highest requirements on the purity of the sample material. Large excess of isobaric contaminants, most notably of the stable chromium isotope  $^{53}\text{Cr}$ , can drastically reduce the precision of the mass spectrometric measurements of  $^{53}\text{Mn}$  or render them completely impossible. Furthermore, due to the limited spectrometry capabilities of LSC, all other radioactive contaminants have to be removed from the sample in order to attribute the detected decays to  $^{53}\text{Mn}$  exclusively.

One possibility to produce the necessary amounts of  $^{53}\text{Mn}$  is to utilize spallation reactions at corresponding accelerator facilities. This involves the preparation and installation of specific targets at accelerator facilities [17]. Amounts in the order of mg of  $^{53}\text{Mn}$ , corresponding to about  $10^{19}$  atoms, were obtained within the ERAWAST initiative from activated beam dump materials at the PSI accelerator complex [17,20,21]. For extracting Mn from the multitude of co-produced long-lived radioisotopes and omnipresent stable isotopes of other elements of the periodic table specific radiochemical separation procedures were worked out at PSI, as described elsewhere [22].

While the bulk of the stable and radioactive impurities in the sample could be removed using conventional chemical separation techniques, this does not apply for the long-lived radioisotope  $^{54}\text{Mn}$  ( $T_{\frac{1}{2}} = 312\text{d}$ ) and for stable  $^{55}\text{Mn}$ . The amount of  $^{54}\text{Mn}$ , which is being co-produced in the spallation processes in a similar quantity as  $^{53}\text{Mn}$ , corresponds to an activity surplus of about 7 orders of magnitude at end of the irradiation. After 25 years the  $^{54}\text{Mn}$  activity of initially  $10^{19}$  atoms will be down to about 400 Bq, i.e. less than 1% of the activity of the same amount of  $^{53}\text{Mn}$  atoms. As an EC decaying radionuclide of the same chemical element, the radiation of  $^{54}\text{Mn}$  overlaps the energy range of  $^{53}\text{Mn}$ . As an EC decaying radionuclide of the same chemical element, the accompanying radiation of  $^{54}\text{Mn}$  overlaps the one of  $^{53}\text{Mn}$ . For a precise LSC measurements with a sample size below

$10^{17}$  atoms (equivalent to 600 Bq) of  $^{53}\text{Mn}$ , an efficient suppression of  $^{54}\text{Mn}$  to provide an activity ratio of at least 1000 : 1 ( $^{53}\text{Mn}$  to  $^{54}\text{Mn}$ ) is essential. At the same time, a similar amount of  $^{53}\text{Mn}$  (i.e.  $10^{17}$  atoms or about 600 Bq) is needed for reasonable measurement times. As the overall amount of  $^{53}\text{Mn}$  available to this experiment is limited to few  $10^{18}$  atoms  $^{53}\text{Mn}$  only, an overall efficiency of about 10% of the mass separation process is mandatory.

Laser mass spectrometry was identified as suitable technique to reach the desired sample purity and ensure optimum process efficiency. Resonance ionization mass spectrometry (RIMS) has proven to be the most universal and for the majority of cases also most efficient method for the generation of ion beams [18]. In addition, it avoids ionization of any elemental or molecular isobaric contaminations, reducing total ion load and space charge disturbance in a subsequent mass separation step to a minimum. The method uses element-selective laser resonance ionization, in combination with a mass selection step at a high transmission isotope separator. Today, primary application of laser resonance ionization is found in the field of highly selective and efficient ionization of exotic, most often short-lived radioisotopes at radioactive ion beam facilities, such as CERN-ISOLDE [19]. The main focus of the work described here is the preparation of a suitable sample for  $^{53}\text{Mn}$  half-life measurement at the RISIKO mass separator. This also includes the development and characterization of a suitable ionization scheme.

## 2 Experimental setup

The RISIKO laser mass separation facility is set up around a 30 keV magnetic sector field mass spectrometer of 60° deflection angle and a focal length of 1 m. It is designed for ion beam currents up to 1  $\mu\text{A}$  and provides mass resolving power of  $\frac{m}{\Delta m} \approx 800$ . For universal application along the entire chart of nuclides, it implies a specifically designed laser resonance ionization ion source unit [23]. This set up involves a high repetition rate pulsed laser system with two or three tunable Ti:sapphire (Ti:sa) lasers, specifically designed for RIMS, which were developed at the University of Mainz. These lasers have meanwhile found application at numerous on-line and off-line facilities worldwide for ion production as well as for spectroscopy and analytics, as pointed out in [24–26], where also the lasers are described in detail. The mass spectrometer set-up used for  $^{53}\text{Mn}$  implantation is sketched in Figure 1, while just a brief outline of mass separator and laser system operation conditions and measuring procedure is given below.

Individual samples containing several  $10^{17}$  atoms of  $^{53}\text{Mn}$  dissolved within 20–60  $\mu\text{L}$  of diluted nitric acid were dripped onto  $10 \times 10\text{ mm}^2$  or  $10 \times 15\text{ mm}^2$  sized, 4  $\mu\text{m}$  Ti carrier foils, dried and calcinated at 220 °C to transform manganese into the oxide form. The Ti foils were folded to a small envelope for full sample enclosure and afterwards introduced into the reservoir of the laser ion source unit. The latter is a Ta capillary of about 120 mm length with an inner diameter of 1 mm, closed near the hottest spot

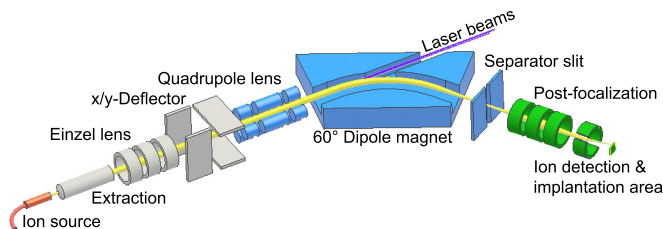


**Fig. 1.** Experimental setup used for the efficiency measurements using  $^{55}\text{Mn}$  and the implantation of  $^{53}\text{Mn}$ .

in the middle by crimping. At the open side it is attached to the rear end of a Ta atomizer/ionizer cavity of 35 mm length and 2.3 mm inner diameter, wherein the laser resonance ionization process takes place. Both, the capillary as well as the cavity, can be heated independently up to temperatures of 2300 K by dc electric currents. These also provide a weak electric field gradient for guiding the generated ions towards the orifice for extraction. By gradually heating the capillary up to the similar maximum temperature as the cavity the fully oxidized  $\text{MnO}_2$  is dissociated by multiple surface contacts with the Ti. The resulting Mn atoms diffuse steadily into the hot atomizer cavity, which is kept at a temperature of about 2300 K throughout the entire measurement. In this way adsorption of sample material on cold spots and corresponding losses are prevented. Within the atomizer cavity the Mn atoms are ionized, predominantly by the laser radiation, which is entering along the beam path through a window in the magnet. Interfering non-selective ionization processes can occur to a significantly lower extent too, e.g. on the hot ion source surfaces or by collision.

An ion beam of up to  $1\ \mu\text{A}$  is extracted by the 30 kV acceleration potential and is well collimated by an einzel lens and a quadrupole lens. After passing the sector field dipole magnet, the separated ion beam passes an adjustable slit which is set to transmit more than 90% of the ions of the selected mass while suppressing neighboring and other masses by at least a factor of  $5 \times 10^3$  in the mass range of Mn. A post focalization lens downstream was used to focus the beam to a size of 5–10 mm FWHM in the target area, where it is finally accumulated in a Faraday-cup like collector structure. The collection foils of about 50 mm diameter can be placed for ion implantation, while an absolute read-out of the ion beam current is achieved on a sensitive electrometer throughout the implantation process. The measured current is used to control the heating of the sample reservoir and to stabilize the ion beam current on an initially specified value.

The three Ti:sa lasers, required for the excitation ionization process, are pumped by about 12 W pump power each from a pulsed frequency-doubled Nd:YAG laser, operating at 532 nm with 10 kHz repetition rate. They can generate tunable laser radiation from 690 nm to 960 nm with an average power up to 4 W. Single pass frequency doubling in a BBO crystal is used to generate the required wavelengths in the blue spectral range. For the preparatory atomic spectroscopy investigations to identify a strong auto-ionizing (AI) state, a specific Ti:sa laser type was

used, which was optimized for continuous wavelength tuning along the entire spectral range by installation of a grating as frequency selective element [27].

### 3 Laser resonance ionization of Mn

In the laser resonance ionization process, atoms of the desired element are excited stepwise along strong optical atomic transitions into auto-ionizing states or directly into the ionization continuum by powerful pulsed laser radiation. Due to the uniqueness of the atomic structure of each element, this process is explicitly element-selective while being highly efficient at the same time. On the other hand, laser ionization schemes have to be developed individually for each element and laser type. A steadily increasing number of presently more than 60 elements are accessible by laser resonance ionization, as listed on a specific database hosted at CERN [28].

For efficient and selective ionization of Mn, a dedicated optical excitation scheme was developed, as visualized in Figure 2. In contrast to earlier Mn ionization schemes using either dye [29] or Ti:sa lasers [30], the use of UV radiation was avoided, which is advantageous in matters of simplicity of the laser setup, the available laser power and the prevention of any non-specific background by the high energy UV laser radiation. From the  $3d^5 4s^2\ ^6S_{5/2}$  ground state [31] the strong transition at 403.2 nm into the  $3d^5(^6S)4s4p(^3P^o)\ ^6P_{7/2}^o$  level at  $24\,802.25\ \text{cm}^{-1}$  was used as a first excitation step. A second step at 446.2 nm further excites the atoms into the second excited level  $3d^5 4s(^7S)4d^6 D_{7/2}$  located at  $47\,212.06\ \text{cm}^{-1}$  [32]. To search for a suitable ionizing transition, the wide-range tunable laser was scanned to access the spectral range from  $59\,800\ \text{cm}^{-1}$  to  $61\,500\ \text{cm}^{-1}$  around the ionization potential (IP), located at  $59\,959.56\ \text{cm}^{-1}$ . The full spectrum is given in Figure 2 (top), exhibiting on the left side numerous sharp Rydberg resonances converging towards the IP as well as a rather smooth behaviour above the IP. At an total energy of  $60\,939.09\ \text{cm}^{-1}$  a significant peak with a resonance enhancement by a factor of five compared to non-resonant ionization was observed, which was identified to correspond to the  $3d^5(2D)4s4p(^3P^o)\ ^4F_{9/2}^o$  auto ionizing level, tabulated at  $60\,938.97\ \text{cm}^{-1}$  [32]. This level exhibits a strongly asymmetric profile, described by a Fano profile [33,34], as shown in the inlay of the spectrum of Figure 2, and was chosen for the third excitation step of the ionization scheme. For the two lower excitation steps, line profiles are given for different laser powers in Figure 2 (lower left). The line widths amount to a minimum of 10 GHz for the lowest laser power and can reach maximum values of well beyond 30 GHz for elevated power levels. These significant peak broadenings and the flattening of the peak profiles display strong saturation in both lower excitation steps, in contrary to the third excitation into the AI level, which is far off from saturation even at maximum available laser power of 2 W. A further increase in laser power could correspondingly increase the ionization efficiencies discussed below. Both isotopes  $^{55}\text{Mn}$  as well as

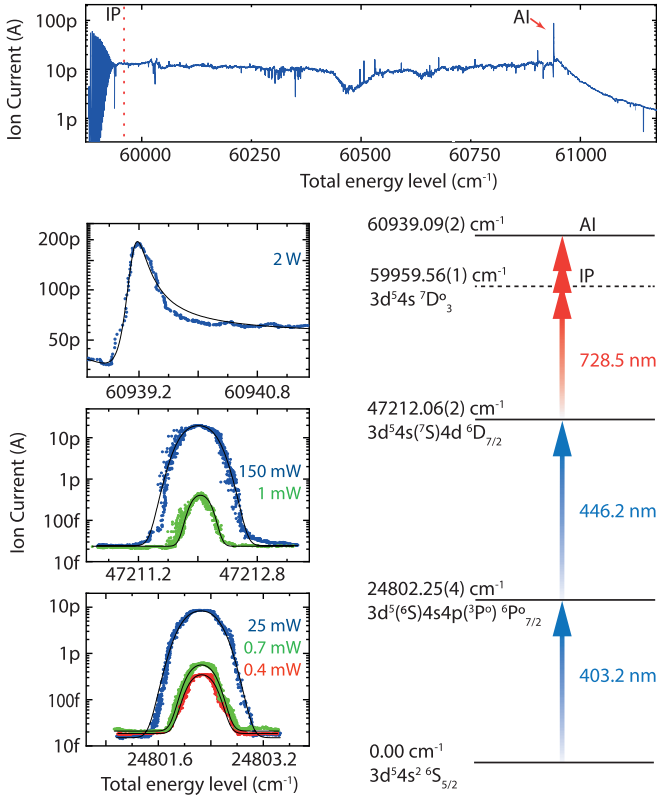


**Fig. 2.** Details of the optical resonance ionization, lower right: three step excitation scheme, lower left: resonance curves of all three excitation step for different laser powers, top: ionization spectrum by tuning of the third excitation step, showing Rydberg resonances converging towards the ionization potential (red dashed line indicated IP) and the used strong autoionizing level at  $60\,939.09\text{ cm}^{-1}$  (indicated AI).

$^{53}\text{Mn}$  exhibit rather large hyperfine splittings in their resonance lines in the order of 10 GHz, which were studied e.g. by Basar et al. [35] In contrast, the optical isotope shifts are known to be very small with values around a maximum of 0.5 GHz in this region of the nuclear chart. As indicated by the absence of any significant asymmetry in a resonance line, all profiles fully cover the hyperfine structures, which are not resolved at all. Correspondingly, no specific laser tuning for excitation of either  $^{55}\text{Mn}$  or  $^{53}\text{Mn}$  was necessary and the ionization probability is assumed to be identical for both isotopes.

## 4 Characterization of the overall efficiency

Tests on samples with well calibrated amounts of stable manganese ( $^{55}\text{Mn}$ ) with atom numbers in the range of  $10^{14}$  to  $10^{16}$  atoms, prepared from an atomic absorption standard solution (Alfa Aesar), were performed with identical sample preparation for characterization of the ion beam production and transport. The efficiency of the Mn implantation is defined as

$$\epsilon = \frac{N_{\text{det}}}{N_0} = \frac{Q}{e \cdot N_0} \quad (2)$$

where  $Q$  is the total accumulated charge in the target,  $N_0$  the number of sample atoms,  $N_{\text{det}}$  the number of detected atoms and  $e$  the elemental charge. Uncertainties in the initial sample size represent one substantial contribution to the efficiency measurement error. They amount to a maximum of about 10% for the test samples with  $10^{14}$  atoms with slightly lower values of a few %, for  $10^{15}$  atoms and for  $10^{16}$  atoms. A second significant uncertainty for the measured efficiency results from imperfections in the ion current measurements at the detector. While sputtered electrons are rather efficiently suppressed by a repeller electrode at the Faraday cup detector, also significant ion sputtering occurs at the 30 keV implantation process. The effect is depending on the surface composition of the implantation target, which varies during the measurement but in most cases is leading to too low recorded currents. Characterization studies showed, that the ion current - and in this way the efficiency - is systematically obscured by deviations in the range of  $-5\%$  up to  $+20\%$ . Subsequently, the systematic uncertainty is indicated by  $\left\{ \begin{smallmatrix} +20 \\ -5 \end{smallmatrix} \right\}$ .

A total of 10 efficiency measurements were performed with different sample sizes and different maximum ion currents. The maximum available laser powers in the range of 25, 150 and 2000 mW were used for the three consecutive excitation steps. Comparable laser settings were used for the implantation runs. After each measurement, a blank Ti sample carrier was heated in the ion source to quantify and verify the Mn traces in the foil and ensured that no significant share of previous measurements remained in the source. In all carrier foils, Mn could be detected. This contribution was ascribed to intrinsic content of the carrier material itself. From these “blank” measurements, an offset for each efficiency measurement was calculated using equation (2). Considering the different sample sizes, this results in a small contribution of  $-0.3(1)\%$  for samples with  $10^{16}$  atoms and  $-6(2)\%$  for  $10^{14}$  atoms, respectively.

An overview of the results is shown in Table 1, where the offset corrections mentioned are included in the reported efficiencies. Optimal operating conditions for the implantation were found at lower ion currents in the range below 100 nA. Samples containing  $10^{14}$  atoms were measured at ion currents of 10 nA, with a typical measurement duration up to significant signal decline of 30 minutes. The typical total release time was 1.5–2 h. For samples with  $10^{15}$  atoms, the source was operated at a similar ion current for some hours. The similar duration in the small and medium sample efficiency measurements, despite similar  $I_{\text{max}}$ , are due to the circumstance that the ion source was heated very slow and careful, so that the entire measurements were dominated by the long heating phase.

Higher currents well beyond 100 nA were used in the measurements with  $10^{16}$  atoms to obtain comparable sampling durations. In this setting, a slight decrease in the efficiency was observed, caused by a less efficient reduction process in the ion source. In addition space charge effects impair the ion beam quality and lead to lower overall transmission through the apparatus. Also, the increased vapor pressure inside the ion source at necessarily raised

**Table 1.** Overview on the efficiency measurements with stable  $^{55}\text{Mn}$  using different sample sizes ( $N_0$ ) and maximum ion currents in the range of 10 nA to 500 nA. The efficiency was calculated using equation (2). The combined standard uncertainty is calculated based on the uncertainties of the sample preparation as well as the ion detection process. The error in the mean  $\bar{\epsilon}$  value is the standard deviation in the set of individual measurements.

| run | $N_0$     | $I_{\max}$ (nA) | time (h) | $\epsilon$ (%)                                                          | $\bar{\epsilon}$ (%) |
|-----|-----------|-----------------|----------|-------------------------------------------------------------------------|----------------------|
| 1   | $10^{14}$ | 10              | 1.6      | $26(2)\left\{\begin{smallmatrix} +5 \\ -1 \end{smallmatrix}\right\}$    | 23(7)                |
| 2   | $10^{14}$ | 10              | 1.7      | $33(3)\left\{\begin{smallmatrix} +7 \\ -2 \end{smallmatrix}\right\}$    |                      |
| 3   | $10^{14}$ | 10              | 2.2      | $23(2)\left\{\begin{smallmatrix} +4 \\ -1 \end{smallmatrix}\right\}$    |                      |
| 4   | $10^{14}$ | 10              | 1.5      | $12(1)\left\{\begin{smallmatrix} +2 \\ -1 \end{smallmatrix}\right\}$    |                      |
| 5   | $10^{15}$ | 20              | 1.3      | $15(1)\left\{\begin{smallmatrix} +3 \\ -1 \end{smallmatrix}\right\}$    | 17(2)                |
| 6   | $10^{15}$ | 10              | 2.3      | $19(1)\left\{\begin{smallmatrix} +4 \\ -1 \end{smallmatrix}\right\}$    |                      |
| 7   | $10^{15}$ | 10              | 1.3      | $18(1)\left\{\begin{smallmatrix} +4 \\ -1 \end{smallmatrix}\right\}$    |                      |
| 8   | $10^{16}$ | 500             | 2.2      | $8.8(3)\left\{\begin{smallmatrix} +2 \\ -0.5 \end{smallmatrix}\right\}$ | 7(2)                 |
| 9   | $10^{16}$ | 500             | 1.0      | $5.8(4)\left\{\begin{smallmatrix} +1 \\ -0.3 \end{smallmatrix}\right\}$ |                      |
| 10  | $10^{16}$ | 500             | 1.3      | $9.7(4)\left\{\begin{smallmatrix} +2 \\ -0.5 \end{smallmatrix}\right\}$ |                      |

reservoir temperature leads to a higher release of sample material from the atomizer region into the extraction region and the mass separator, similarly causing possible loss of Mn atoms. The result is the observation of a reduction in the achievable efficiency. Nonetheless, it should be noted that an increase in the ion current by a factor of 50 leads to a loss in efficiency by a factor of about 3, so that high-current operation could still be foreseen for less valuable samples and for implantation of macroscopic amounts.

## 5 Implantation of $^{53}\text{Mn}$

In order to reveal possible charged particle contaminations in the ion beam, which may affect the beam quality and the implantation process, the implantation runs were preceded by a mass spectrometric analysis in the full mass range from 20 u to 75 u taken at a typical ion source temperature from more than 1300 °C during implantation. Figure 3 compares two mass spectra, the upper one with resonance ionization on Mn and the lower one with lasers blocked. The latter one shows just unselective ionization of volatile species, e.g., by surface ionization at the hot walls of the ion source which addresses primarily alkaline and alkaline earth elements, delivering beam currents up to 100 nA. Weak contributions of transition metals like Ti and its monoxide, well below 1 nA, are also visible, indicated by its specific isotope pattern. Additional unresolved background structures occurring in the low pA range are ascribed to organic compounds or doubly charged molecules. By introducing resonance ionization, the mass peaks of Mn are increased by about a factor of  $10^5$  to ion currents of typically 100 nA. The signal of  $^{53}\text{Mn}$ , relevant for the implantation process, exceeds the unspecific background on this mass by a factor of more

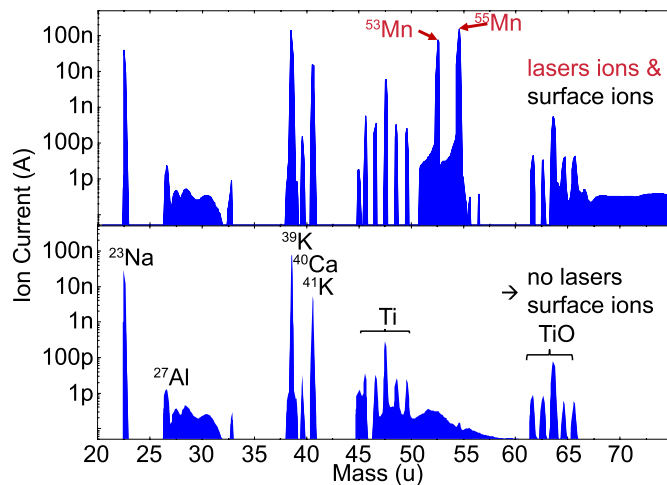


**Fig. 3.** Comparison of mass spectrum in the range from 20 u to 75 u (upper panel) with and without resonance ionization of Mn (lower panel).

than  $3 \times 10^4$ . Most conservatively ascribing any background entirely to  $^{53}\text{Cr}$ , a suppression of this elemental isobaric interference of at least 4 orders of magnitude to non-relevant amounts is demonstrated. The remaining contribution from the stable isotope  $^{55}\text{Mn}$  on the mass of  $^{53}\text{Mn}$  amounts to about  $1 \times 10^{-4}$ , corresponding to a selectivity one order of magnitude higher than requested, while no measurable amount of  $^{54}\text{Mn}$  is observed. As expected, most of the other mass peaks are unaffected by the laser radiation, while just the Ca, Ti (which was introduced as carrier foil) and TiO signals show a slight gain of about a factor of 10, which is either due to the increased heating by the laser radiation or to non-resonant ionization of highly excited atoms, stemming from gas collisions in the hot source environment.

Total Mn atom sample loads in the ion source in all cases remained below  $10^{18}$  atoms. For the implantation runs, the mass separator was operated with a mean ion current well below 100 nA on the selected mass of 53 u, which corresponds to an overall ion current of about 400 nA at the ion source exit and in front of the magnet. At this level disturbing space charge effects are still reasonably low. Post focalization was used to shape the circular ion beam spot to a size of approximately 7.5 mm at the target stage. This spot was slowly scanned over the predefined circular central collection area of 12 mm diameter. For easy handling the Al-target diameter was 52 mm, being covered outside the active area by an aperture. Figure 4 shows on the left the homogeneity of the ion current during the scan over this implantation area as function of the lateral deflection. A photo of the Al foil target after the successful implantation is shown in Figure 4 on the right, where the implanted  $^{53}\text{Mn}$  is well visible as central dark spot.

An upper limit for the density of implanted ions on the predefined area of  $\sim 180 \text{ mm}^2$  is resulting from sputtering losses, which occur due to the bombardment of the incoming 30 keV ions. This value was estimated for Al as well as for  $\text{Al}_2\text{O}_3$  being the most likely expected

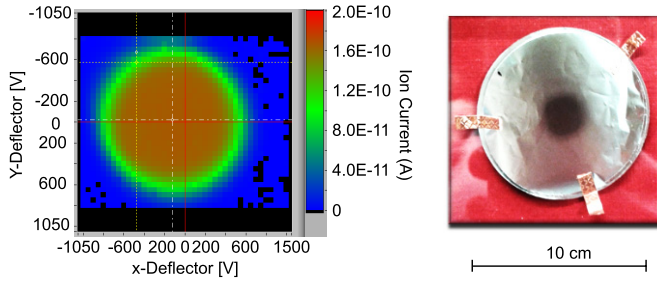


**Fig. 4.** Implantation of  $^{53}\text{Mn}$  in Al (T2). **Left:** view of the accumulated ion current distribution during the implantation **Right:** Al foil target with central implantation of  $^{53}\text{Mn}$ .

surface material layers, by the program code TRIDYN [36], which gives maximum achievable atom densities and implantation depth for the process, as shown in Figure 5.

In both materials Al and  $\text{Al}_2\text{O}_3$ , about 1 to  $1.5 \times 10^{17}$  atoms can be maximally implanted into the area of  $\sim 180 \text{ mm}^2$  corresponding to the collection spot size. The implantation depth in Al for Mn ions of 30 keV is about 20 nm, which has to be compared to the  $\text{Al}_2\text{O}_3$  surface layer thickness of about 5 nm [37]. Thus, the majority of Mn ions are implanted into the Al bulk material as shown in Figure 5. An upper limit of about  $1 \times 10^{17}$  atoms per target area was respected during the  $^{53}\text{Mn}$  implantation runs, which meets the specification of the requested purification and enrichment as discussed in the introduction.

For a conservative safety margin, the total initial sample amount of  $\sim 1.4 \times 10^{18}$  atoms of  $^{53}\text{Mn}$  was distributed into 6 subsamples. Out of these, 5 samples could be properly purified and implanted; including one test sample of just  $1 \times 10^{17}$  atoms and two times two samples of either  $2 \times 10^{17}$  or  $3 \times 10^{17}$  atoms of  $^{53}\text{Mn}$  each, respectively. During implantation of a sixth sample a fatal mechanical error occurred at the mass separator implantation stage, which lowered the achievable efficiency down to 2.7%. This run was thus abandoned. Each sample contained a surplus of about a factor of 2 of stable  $^{55}\text{Mn}$ , as visible in Figure 3. The five samples no. 1 to no. 5 were used for individual implantation runs, from which the three smaller ones, denominated no. 1 to no. 3, were implanted into a first and the two larger ones, no. 4 and no. 5, into a second Al foil target, T1 and T2, respectively. The individual sample sizes in number of initial  $^{53}\text{Mn}$  atoms ( $N_0$ ), durations of implantation run, overall efficiencies achieved for each of the 5 runs are given in Table 2. In all cases, the implanted ion beam current was stabilized at about 100 nA, resulting in acceptable duration of the implantation runs in the order of less than 24 h. In this time frame, suitable operation stability of laser system and mass separator could be guaranteed.

The number of implanted  $^{53}\text{Mn}$  atoms into the two Al targets T1 and T2 amounts to  $8.3(0.7)_{-0.4}^{+2} \times 10^{16}$  and  $7.3(0.6)_{-0.4}^{+1} \times 10^{16}$  atoms, respectively, i.e., to a total of  $1.6(0.1)_{-0.1}^{+0.3} \times 10^{17}$  atoms, which corresponds to an average efficiency of 11.4% for the entire implantation process, significantly lowered by the lost sample.

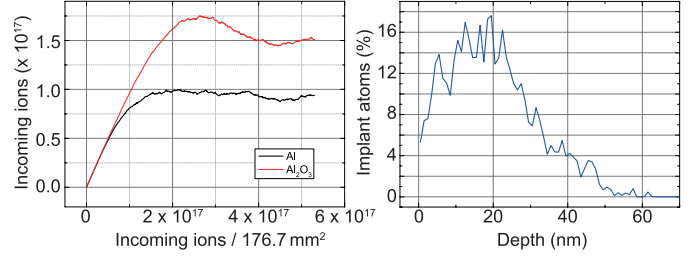


**Fig. 5.** Implantation simulation with the program TRIDYN for Mn ions of 30 keV energy. **Left:** maximum number of implanted atoms for Al and  $\text{Al}_2\text{O}_3$  as function of incoming ion number on the implantation area. **Right:** implantation depths in Al.

**Table 2.** Individual implantation runs, sample size  $N_0$   $^{53}\text{Mn}$  atoms, duration, efficiency of implantation and the number of individually implanted  $^{53}\text{Mn}$  atoms are given. The implantation efficiency ( $\epsilon$ ) was calculated via equation (2). The efficiency uncertainty was determined in the same way as explained in Section 4.

| run no. | $N_0$ [ $\times 10^{17}$ ] | time (h) | $\epsilon$ (%)        | $N_{\text{impl}}$ [ $\times 10^{16}$ ] |
|---------|----------------------------|----------|-----------------------|----------------------------------------|
| 1       | 1                          | 29.5     | 19(2) $\{-1\}^{+4}$   | 1.9(1) $\{-1\}^{+4}$                   |
| 2       | 2                          | 29.6     | 18(2) $\{-1\}^{+4}$   | 3.6(3) $\{-2\}^{+7}$                   |
| 3       | 2                          | 18.5     | 14(2) $\{-0.7\}^{+3}$ | 2.8(2) $\{-1\}^{+6}$                   |
| 4       | 3                          | 22.8     | 12(1) $\{-0.6\}^{+2}$ | 3.6(3) $\{-2\}^{+7}$                   |
| 5       | 3                          | 13.7     | 12(1) $\{-0.6\}^{+2}$ | 3.6(3) $\{-2\}^{+7}$                   |

Considering only the 5 successful runs a value of 14.2% is resulting. Nevertheless, both values very well meet the requested specifications. A precise quantification of the implanted  $^{53}\text{Mn}$  amount will be carried out afterwards by MC-ICP-MS as discussed in the introduction.

## 6 Summary

Resonance ionization mass spectrometry was used for purification and enrichment of the radioisotope  $^{53}\text{Mn}$  including direct implantation into Al foil targets, which were applied for subsequent precision measurements of the half-life of the radioactive decay. As preparation a dedicated optical excitation and ionization scheme for Mn was developed and characterized on quantified samples of stable  $^{55}\text{Mn}$ . Efficiency measurements were performed on different sample sizes and for different ion beam currents from 10 nA up to 500 nA. An average value of  $\sim 23\%$  implantation efficiency was demonstrated for smallest samples of  $10^{14}$  atoms and a very low ion current of 10 nA. Increasing the sample size to  $10^{15}$  atoms resulted in a reduced efficiency of 17%, while either higher atoms numbers of  $10^{16}$  atoms or ion currents up to 500 nA further decreased this value down to 7%. Further more losses resulting from sputtering processes on the Al targets were estimated by simulations and considered in the measurements. Based on these measurements the implantation of about  $1.6(1)_{-1}^{+3} \times 10^{17}$  atoms of  $^{53}\text{Mn}$  was successfully carried out. Ion beam currents of 100 nA on mass 53, corresponding to about 400 nA total ion current in

front of the separator magnet were used for this process, which resulted in an overall efficiency of 14.2%. The implanted amount of about  $1.6 \times 10^{17}$  atoms corresponding to an activity of about 1 kBq of  $^{53}\text{Mn}$  represents a more than sufficient sample size for both, the LSC activity standardization as well as the high precision MC-ICP-MS atom counting. Using the sample material described here, preliminary results of the half-life determination of  $^{53}\text{Mn}$  points to an overall uncertainty of less than 2%, well below the initial goal of 3%. Furthermore, no signal of  $^{54}\text{Mn}$  could be observed in the LSC and hpGe gamma spectra, which confirmed the high effectivity of the RIMS separation. A manuscript summarizing the half-life determination is currently in preparation.

The authors want to thank R. Heinke, P. Naubereit and M. Trümper for their assistance during preparations and/or measurements. The software package TRIDYN, developed by W. Möller, is licensed by Helmholtz-Zentrum Dresden-Rossendorf e. V., Bautzner Landstr. 400, D-01328 Dresden, Germany, represented by the board of directors.

### Author contribution statement

All the authors were involved in the preparation of the manuscript. All the authors have read and approved the final manuscript.

### References

1. A.M. Boesgaard, *Ann. Rev. Astron. Astrophys.* **23**, 319 (1985)
2. R. Wölfle et al., *Radiochim. Acta* **18**, 207 (1972)
3. M. Heimann et al., *Geochim. Cosmochim. Acta* **38**, 217 (1974)
4. M. Honda et al., *Phys. Rev. C* **4**, 1182 (1971)
5. E. Zinner, *Science* **300**, 265 (2003)
6. K. Knie et al., *Nucl. Instrum. Methods Phys. Res., Sect. B* **172**, 806 (2000)
7. M. Poutivtsev et al., *Nucl. Instrum. Methods Phys. Res., Sect. B* **268**, 187 (2010)
8. I. Leya et al., *Meteo. Planet. Sci.* **55**, 818 (2020)
9. L.G. Gladkis et al., *Nucl. Instrum. Methods Phys. Res., Sect. B* **259**, 178 (2007)
10. J.M. Schaefer et al., *Earth Planet. Sci. Lett.* **251**, 334 (2006)
11. G.P. Glasby, in *Manganese: Predominant Role of Nodules and Crusts* (Springer, Berlin, Heidelberg, 2006), pp. 371–427
12. G. Korschinek et al., *Phys. Rev. Lett.* **125**, 031101 (2020)
13. I.D. Hutcheon et al., *Science* **282**, 1865 (1998)
14. R. Dressler et al., *J. Phys. G: Nucl. Part. Phys.* **39**, 105201 (2012)
15. J. Ulrich et al., *Phys. Rev. Lett. C* **102**, 024613 (2020)
16. K. Kossert et al., *Appl. Radiat. Isot.* **64**, 1446 (2006)
17. D. Schumann et al., *EPJ Web Conf.* **146**, 06019 (2017)
18. V.N. Fedoseev et al., *Phys. Scr.* **85** (2012)
19. V.N. Fedoseev et al., *J. Phys. G* **44** (2017)
20. D. Schumann et al., *Radiochim. Acta* **97**, 123 (2009)
21. D. Schumann et al., *J. Phys. B: Nucl. Part.* **35** (2008)
22. M. Ayrano et al., *J. Radioanal. Nucl. Chem.* **286**, 649 (2010)
23. T. Kieck et al., *Rev. Sci. Instrum.* **90**, 053304 (2019)
24. S. Rothe et al., *J. Phys. Conf. Ser.* **312**, 052020 (2011)
25. C. Geppert et al., *Nucl. Phys. A* **746**, 47 (2004)
26. C. Grüning et al., *Int. J. Mass Spectrom.* **235** (2004)
27. A. Teigelhöfer et al., *Hyperfine Interact.* **196** (2010)
28. available: <https://riliselements.web.cern.ch/> (2021)
29. V.N. Fedoseev et al., *Nucl. Instrum. Methods Phys. Res., Sect. B* **126** (1997)
30. Y. Liu et al., *J. Phys. B: At. Mol. Opt. Phys.* **48**, 205205 (2015)
31. J. Sugar et al., *J. Phys. Chem. Ref. Data* **14**, 177 (1985)
32. A. Kramida et al., NIST Atomic Spectra Database available: <https://physics.nist.gov/asd> (2021)
33. U. Fano et al., *Phys. Rev.* **137**, A1364 (1965)
34. K. Ueda et al., *Phys. Rev. A* **35**, 4602 (1987)
35. G. Basar et al., *Phys. Scr.* **67**, 476 (2003)
36. W. Moeller et al., *Nucl. Instrum. Methods Phys. Res., Sect. B* **2**, 814 (1984)
37. B.R. Strohmeier et al., *Surf. Interface Anal.* **15**, 51 (1990)

**Open Access** This is an open access article distributed under the terms of the Creative Commons Attribution License (<https://creativecommons.org/licenses/by/4.0>), which permits unrestricted use, distribution, and reproduction in any medium, provided the original author(s) and source are credited.

**Cite this article as:** N. Kneip, D. Studer, T. Kieck, J. Ulrich, R. Dressler, D. Schumann and K. Wendt, Separation of manganese isotopes by resonance ionization mass spectrometry for  $^{53}\text{Mn}$  half-life determination, *Eur. Phys. J. Appl. Phys.* **97**, 19 (2022)